JACS
JOURNAL OF THE AMERICAN CHEMICAL SOCIETY

ARTICLE

pubs.acs.org/JACS

Distinguishing Homogeneous from Heterogeneous Catalysis in Electrode-Driven Water Oxidation with Molecular Iridium Complexes

Nathan D. Schley,[†] James D. Blakemore,[†] Navaneetha K. Subbaiyan,[‡] Christopher D. Incarvito,[†] Francis D'Souza,[*,‡] Robert H. Crabtree,[*,†] and Gary W. Brudvig[*,†]

[†]Department of Chemistry, Yale University, P.O. Box 208107, New Haven, Connecticut 06520-8107, United States

[‡]Department of Chemistry, Wichita State University, Wichita, Kansas 67260-0051, United States

Supporting Information

ABSTRACT: Molecular water-oxidation catalysts can deactivate by side reactions or decompose to secondary materials over time due to the harsh, oxidizing conditions required to drive oxygen evolution. Distinguishing electrode surface-bound heterogeneous catalysts (such as iridium oxide) from homogeneous molecular catalysts is often difficult. Using an electrochemical quartz crystal nanobalance (EQCN), we report a method for probing electrodeposition of metal oxide materials from molecular precursors. Using the previously reported $[Cp^*Ir(H_2O)_3]^{2+}$ complex, we monitor deposition of a heterogeneous water oxidation catalyst by measuring the electrode mass in real time with piezoelectric gravimetry. Conversely, we do not observe deposition for homogeneous catalysts, such as the water-soluble complex Cp*Ir(pyr-CMe_2O)X reported in this work. Rotating ring-disk electrode electrochemistry and Clark-type electrode studies show that this complex is a catalyst for water oxidation with oxygen produced as the product. For the heterogeneous, surface-attached material generated from $[Cp^*Ir(H_2O)_3]^{2+}$, we can estimate the percentage of electroactive metal centers in the surface layer. We monitor electrode composition dynamically during catalytic turnover, providing new information on catalytic performance. Together, these data suggest that EQCN can directly probe the homogeneity of molecular water-oxidation catalysts over short times.

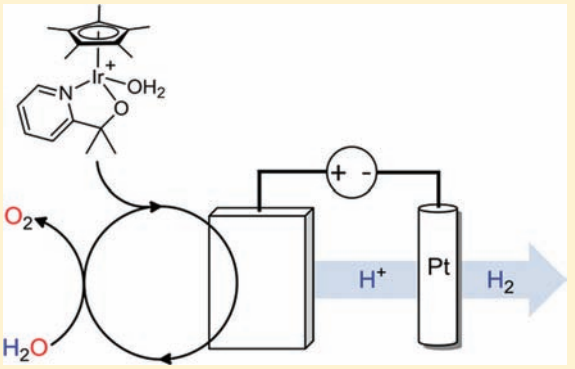

INTRODUCTION

The development of effective water-oxidation catalysts is key to the assembly of electrochemical and photoelectrochemical systems capable of storing reducing equivalents as fuels.[1] Among water-oxidation catalysts, homogeneous molecular systems attract the most attention due to their straightforward synthesis, ease of characterization, and tunable properties. The catalytic mechanism is also more easily investigated in solution.[2] Furthermore, through modification of the ligands, homogeneous catalysts can be incorporated into more complex molecular structures including molecular photosensitizer scaffolds designed to enable solar water splitting.[3]

Heterogeneous catalysts for water oxidation were known long before their homogeneous analogues. This is no doubt due to their thermodynamic stability, high activity, and, in some cases, longevity.[4] Because they are solid-state materials, large-scale preparation is more straightforward, and methods exist for incorporating them into commercial devices such as proton-exchange membrane electrolyzers.[5] Moreover, the preparation of traditional heterogeneous materials can be modified to afford high surface-area bulk materials with nanoscale features that enhance activity.[6,7]

In homogeneous catalysis research, there is a long-standing and perplexing ambiguity as to whether a given catalyst is homogeneous or simply a precursor to a catalytically active heterogeneous material. Our own group has been concerned with this problem for some time.[8,9] A number of methods have been successfully applied to make this distinction for catalytic reduction reactions.[10−12] However, few methods have been reported for distinguishing the homogeneity of oxidation catalysts. In water-oxidation catalysis with organometallic iridium complexes, this is a particular concern, because the highly oxidizing conditions required for oxygen evolution can cause ligand degradation to give iridium oxides, which are known heterogeneous water-oxidation catalysts. Additionally, techniques such as microscopy, kinetic analyses, and catalyst reisolation experiments are complicated by the dilute aqueous conditions and high salt concentrations often used for these highly active catalysts.

We have recently reported a number of Cp and Cp* iridium complexes that are highly active for water-oxidation when driven with a chemical oxidant.[13,14] All indications favor a homogeneous origin for catalysis at short times with half-sandwich complexes having chelate ligands such as 2-phenylpyridine or 2,2′-bipyridine,[14] though we cannot exclude the formation of

Received: January 17, 2011
Published: June 15, 2011

catalytically active iridium oxides as a contributing factor at longer reaction times. Conversely, we have recently reported that the tris-aqua complex (**1**) (Figure 1) shows a unique response upon electrochemical oxidation, forming an amorphous blue layer of iridium oxide material (**BL**) which is a robust heterogeneous water-oxidation catalyst.[15] This observation highlights the importance of careful investigations of catalyst homogeneity in this family of iridium complexes, and indeed in all homogeneous catalysts for water oxidation.

We now report a method for probing the homogeneity of water-oxidation electrocatalysts using an electrochemical quartz crystal nanobalance (EQCN) to conduct piezoelectric gravimetry as water oxidation is taking place. In the case of heterogeneous catalyst formation, a mass change occurs as catalyst material is deposited on the electrode surface. Under these conditions, a truly homogeneous catalyst gives no such mass change at the electrode.

RESULTS

In order to test this method for determining homogeneity, we compared the behavior of Cp*Ir compounds **2** and **3**, bearing the 2-(2′-pyridyl)-2-propanolate ligand, to the previously reported tris-aqua complex **1**.[16,17] The new compounds **2** and **3** were prepared from $[Cp^*IrCl_2]_2$ by treatment with 2-(2′-pyridyl)-2-propanol and sodium bicarbonate in refluxing acetone. Compound **3** was then obtained from **2** by anion metathesis with silver trifluoroacetate in water.

X-ray crystal structures were obtained for **1**, **2** and **3** (Figure 2). For complex **1**,[18] the structure obtained by crystallization from water shows the sulfate counterion in the outer sphere, with three water molecules in the inner sphere forming an extended hydrogen-bonding network with the solvent water and anion. The structures of **2** and **3** confirm the expected connectivity and show that the chelate ligand gives rise to a stable iridium alkoxide. The 2-(2′-pyridyl)-2-propanolate ligand was expected to be strongly electron donating as in the case of our previously reported cyclometalated 2-phenylpyridine analogue.[13] Unlike the 2-phenylpyridine case, however, the pyridyl-alkoxy ligand provides additional oxygen lone-pairs adjacent to the metal and confers excellent water solubility to the resulting iridium complexes, allowing for complete electrochemical characterization in aqueous solution.

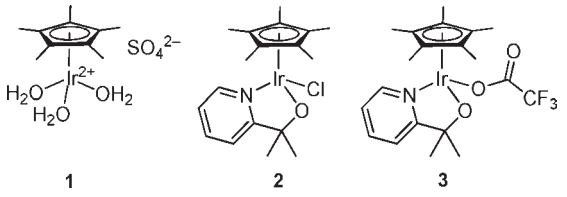

Figure 1. Structures of **1**, **2**, and **3**.

UV−vis experiments on **2** and **3** in aqueous solution strongly suggest that the chloride and trifluoroacetate ligands have dissociated, in contrast to the solid state structures. Both complexes appear red in concentrated aqueous solutions, and in dilute solution have similar UV−vis spectra (Figure 3). Addition of a large excess of sodium chloride to an aqueous solution of **2** gives a color change to orange, and UV−vis analysis of such solutions shows that increasing chloride concentration causes a decrease in the intensity of the signals at λ = 521 and 382 nm and an increase in intensity at 370 nm with an isosbestic point at 378 nm. In solutions of 0.5 M NaCl, **2** and **3** give essentially identical UV−vis spectra, consistent with the suggestion that, in aqueous solutions, water competes with chloride for metal binding. Complex **2** has an apparent dissociation constant (K_d) of 80 mM at pH 7, and no pH change occurs in unbuffered solutions upon chloride addition. Nitrate ligation can be ruled out in the case of potassium nitrate, the electrolyte used in the electrochemical studies, as no change is observed in the UV−vis spectrum of **2** up to at least 0.5 M KNO_3.

Catalytic Oxygen Evolution. We next turned to the catalytic properties of **3**. Because electrochemical oxidation of chloride to hypochlorite or chlorine is possible (a competing reaction with oxidation of water to dioxygen, depending on pH and cell conditions), only **3** was examined for water-oxidation activity. Stationary-electrode cyclic voltammetry of **3** in aqueous solution shows only an irreversible, catalytic response with an onset near 1.0 V vs NHE (see Figure 4). The appearance of the oxidation wave and its irreversible nature are consistent with oxygen evolution ($E^{\circ\prime}$ = 820 mV at pH 7), but in order to establish water oxidation with certainty we moved to measure the oxygen product directly by rotating ring-disk electrode (RRDE) electrochemistry and Clark-type oxygen electrode experiments.

RRDE electrochemistry is conducted in a hydrodynamic, four-electrode configuration. The technique is useful here, because product oxygen generated electrochemically at the disk electrode is swept to and detected at the ring electrode as current corresponding to reduction of O_2 to H_2O_2. However, the

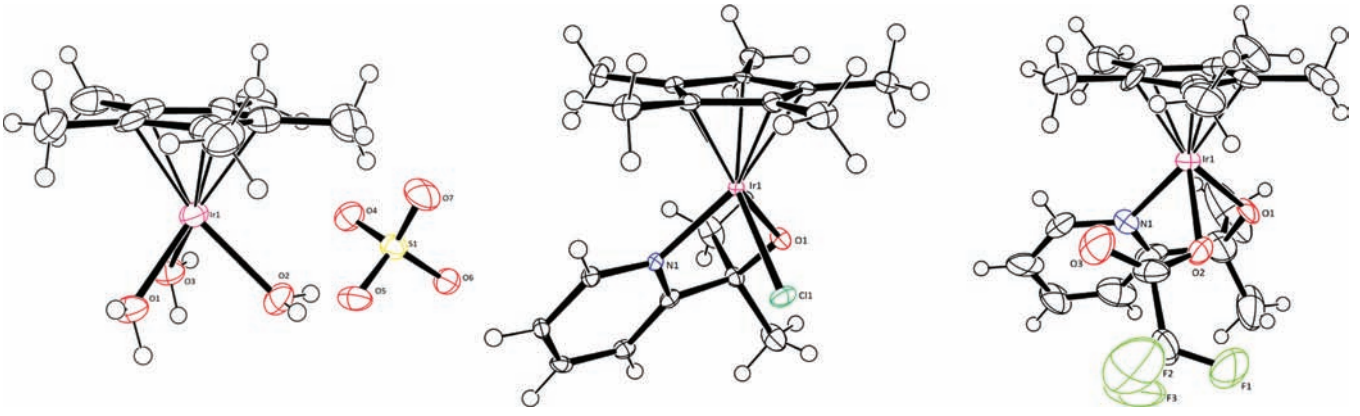

Figure 2. ORTEP drawings of crystal structures of **1** (left), **2** (center), and **3** (right) with ellipsoids shown at 50% probability. Solvent molecules have been omitted for clarity.

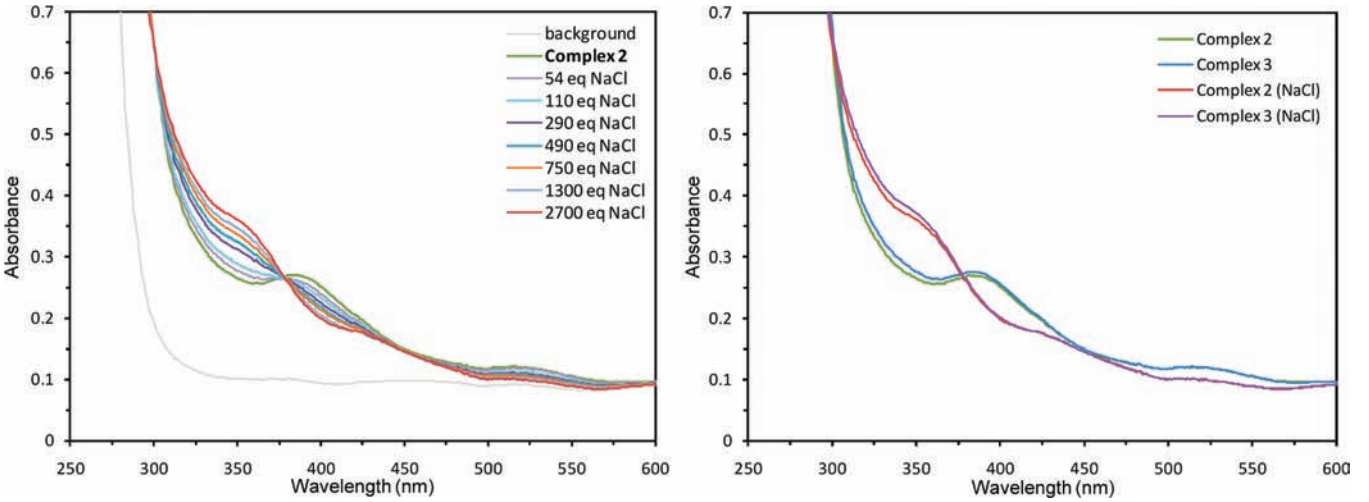

Figure 3. UV−vis spectra of **2** with increasing chloride concentration (left). Comparison of UV−vis spectra of **2** and **3** in deionized water and **2** and **3** in 0.5 M NaCl (right).

technique is most often applied to catalytic systems in which product is measured at the ring electrode after production at a *disk surface-attached* catalyst. In our case, the catalyst is dissolved in the bulk solution and freely diffusing. Therefore, ring currents (from reduction chemistry) could correspond to any of the following: catalytic intermediates, products of partial water oxidation (e.g., H_2O_2), catalyst decomposition products, or oxygen.

With all these caveats, we were still enthusiastic about applying the technique to complex **3**, since we can gain key information about the ultimate fate of oxidizing equivalents delivered by the oxidizing potential. Therefore, in our first experiment, we set the ring potential to −300 mV, a sufficiently reducing potential so as to allow reduction of oxygen, hydrogen peroxide, and potentially also oxidized iridium intermediates. We then swept the disk potential through multiple complete on−off cycles of the oxidation chemistry. The results for **3**, shown in Figure 5, are presented in the format used by Fontecave and co-workers.[19]

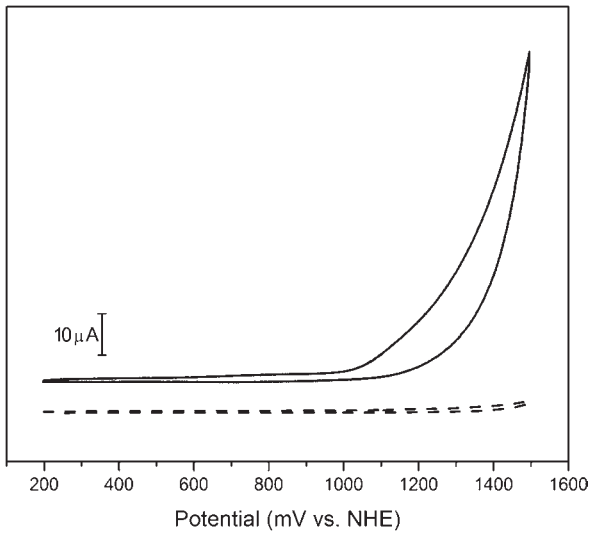

Figure 4. Cyclic voltammetry of **3** at a basal plane graphite electrode. Solid line: 3.3 mM **3**. Dashed line: electrolyte background. Conditions: 0.1 M KNO_3 supporting electrolyte; pH 7; scan rate, 20 mV/s.

The RRDE results in Figure 5 show that electrochemical oxidation of complex **3** (disk current) results in generation of freely diffusing oxidized species. From the data, it is clear that the disk (oxidation) current and ring (reduction) current show onset at essentially the same time, indicative of chemistry occurring at the disk electrode, rather than oxygen or other reducible species already present in the system. Our group has used basal-plane graphite electrodes for many years owing to their well-known low background current levels, especially in comparison with noble metal electrodes such as platinum.[14,15,20,21] Essentially no oxygen or diffusing oxidized species were detected in the background runs, which is consistent with low catalytic efficiency of the bare basal-plane surface. The lack of diffusing oxidized species in the background is also consistent with oxidative processes taking place on the bare graphite surface, consistent with our previous observations of progressive damage to basal-plane graphite electrodes under oxidizing conditions.

Upon observing a ring current which was dependent upon oxidation occurring at the disk, we next moved to determine the voltage dependence of the ring current to help identify the species undergoing reduction at the ring. The resulting polarization curve (collected with the disk polarized to 1.46 V, see the Supporting Information) shows only a single reduction event, with onset at −0.1 V. This is consistent with reduction of dioxygen, which occurs near 0 V regardless of pH conditions.[22] Notably, we do not see evidence of any electrochemically reversible cathodic features associated with the apparently irreversible process seen in single-electrode cyclic voltammetry. Since the transit time for our ring-disk configuration and chosen experimental parameters is expected to be 200 ms at a minimum (average transit time: 500 ms disk-to-ring), we would not see very short-lived intermediates at the ring.[23] However, the RRDE technique as applied here gives us additional information not available otherwise. Specifically, we probe at very short times and with good sensitivity, avoiding complications from either interfering signals or conversion of the catalyst precursor into other materials.

In order to confirm that oxygen is produced by our catalyst precursor **3**, we also measured oxygen evolution with a Clark-type electrode. We constructed a two-chamber glass electrochemical cell equipped with the appropriate connections for our working, reference, and counter electrodes as well as the Clark-type

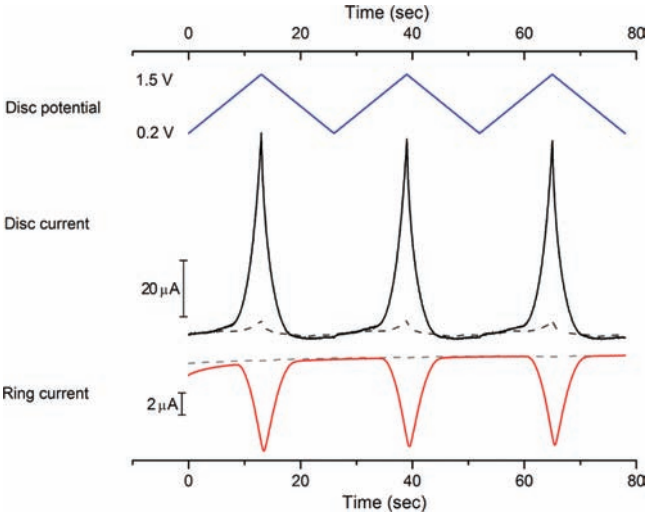

Figure 5. RRDE cyclic voltammetry results for **3** as a function of time. Blue line: applied disk potential. Black solid line: disk current observed with **3**, corresponding to current at the oxidizing electrode. Dark gray dashed line: disk background current. Red solid line: ring current observed with **3**, corresponding to reduction of oxidized, diffusing species. Light gray dashed line: disk current in absence of catalyst. Conditions: 3.3 mM **3**; basal plane graphite disk; Pt ring; scan rate, 100 mV/s; rotation rate, 700 rpm; approximate volume of solution, 12 mL; cell was purged with nitrogen for 30 min prior to beginning the voltage sweeps. For details, see the Experimental Section.

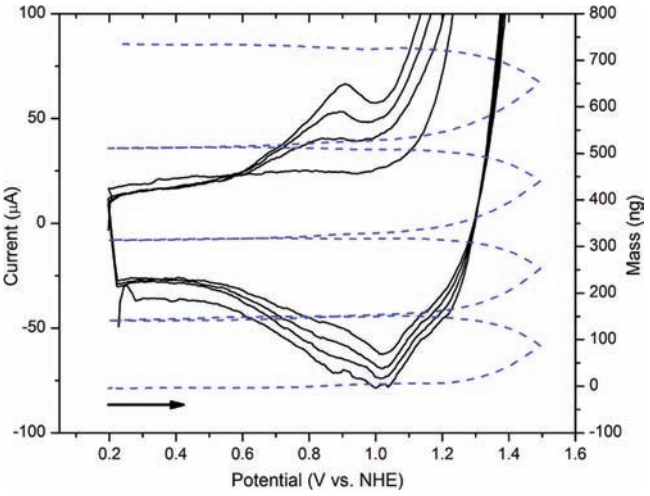

Figure 6. Response of compound **1** in EQCN experiment (four cycles of voltammetry). Black solid line: cyclic voltammetric response recorded by potentiostat. Dashed blue line: mass change recorded by nanobalance. Conditions: 0.1 M KNO_3, pH 2.9, 3 mM **1**. Scan rate: 50 mV/s.

electrode for measuring dissolved oxygen. The Clark electrode provides excellent detection sensitivity which gives a clear signal down to tens of nanomoles of oxygen in our configuration with rapid (<20 s) time response. In a typical experiment with **3**, we passed sufficient current to generate 111 nmol of oxygen. In real time, we then monitored a rise in the dissolved oxygen content of the solution. The Clark electrode detects the production of 70 nmol of oxygen. In the absence of **3**, some oxygen is produced by the gold oxide surface of the electrode, but the observed charge transferred (sufficient for production of 69 nmol of O_2) and amount of oxygen detected (36 nmol) are substantially decreased. (See the Supporting Information for details.) After use in a solution of **3**, the electrode was rinsed and transferred to a fresh "blank" KNO_3 solution, where a new background test gave results consistent with the original background activity and substantially lower than when **3** is present. This indicates that no catalytic deposit is present on the surface.

The oxygen detection from these experiments confirms that our precursor **3** is active for water oxidation catalysis, producing approximately 60 nmol O_2 min^{-1} cm^{-2} at the gold electrode surface after correction for the background. The yield of oxygen detected is less than 100%, but similar to the faradaic yield (ca. 60−70%) obtained by water oxidation using the gold surface in the absence of **3**, suggesting that the inefficiencies which contribute to suboptimal oxygen yield are intrinsic to the system and not a result of substantial current being used for ligand oxidation. Side reactions are of concern, since our catalyst **3**, and others, contain sensitive C−H bonds like the methyl groups on the Cp* ligand, that are normally more easily oxidized than water. Indeed, oxidative reactions of these methyl groups have been reported.[24] Additionally, incomplete oxidation of the catalyst to an intermediate oxidation level as in a recently characterized iridium(IV) analogue[25] could contribute to a reduction in faradaic efficiency if the intermediate diffuses away from the electrode prior to subsequent oxidation.

The confirmation that oxidizing equivalents are converted into oxygen is key. First, the complex **3** is a competent catalyst precursor for water oxidation when driven with an electrode. Second, the conversion of oxidizing equivalents into oxygen strongly suggests that side reactions, such as decomposition of the catalyst precursor **3**, are a small contribution to the chemistry taking place when **3** is oxidized electrochemically. With the catalytic properties of **3** thus established, we turned to electrochemical piezoelectric gravimetry to further probe the electrochemical behavior of **3** and **1**.

Electrochemical Quartz Crystal Nanobalance Studies. EQCN relies on the converse piezoelectric effect to monitor mass changes at the surface of the working electrode during an electrochemical experiment, and is discussed in detail elsewhere.[26] Briefly, if a mass change or change in the viscoelasticity of the contacting medium occurs at the surface of the piezoelectric working electrode, then the frequency of the resonant vibration will shift depending on the magnitude and sign of the change in mass. The Sauerbrey equation relates this change in frequency to the exact change in mass of the electrode, assuming there are no major viscoelastic effects.[27] EQCN is exceptionally sensitive and allows for mass changes and other processes on the surface to be monitored down to the level of nanograms per square centimeter. It has been shown by Birss et al., and others, that electrochemical piezoelectric gravimetry can successfully detect mass changes taking place during iridium oxide formation on a surface of sputtered iridium metal.[28] Importantly, high quality data have been collected on thin iridium oxide layers.[29]

We used a conventional three-electrode configuration with a gold-coated quartz crystal serving as the working electrode connected to the nanobalance electronics (platinum foil counter electrode; Ag/AgCl reference electrode). Before running the experiments on compounds **1** or **3**, extensive background cyclic voltammograms were collected to condition the gold surface to uniformity. Nonetheless, and not surprisingly, the gold surface

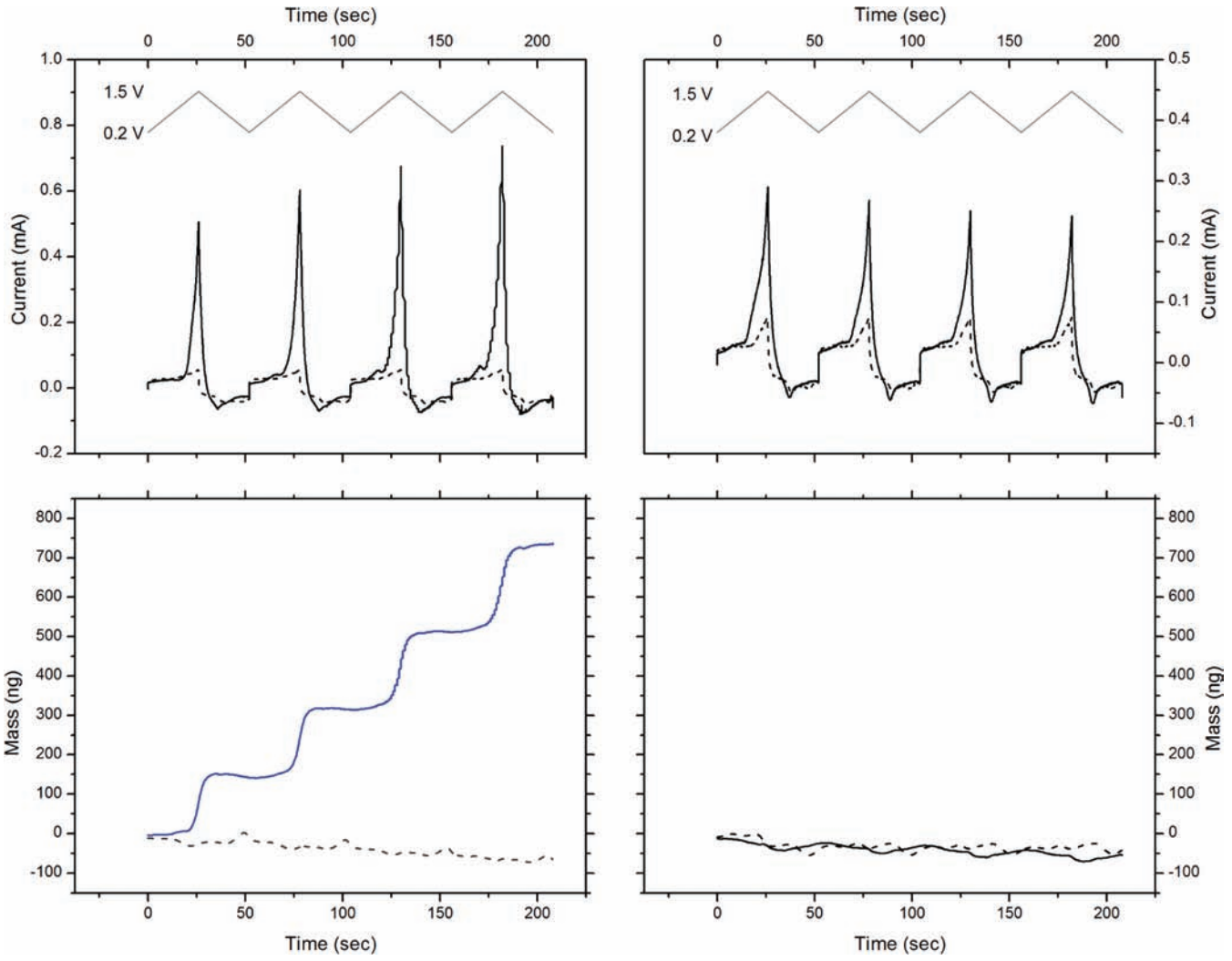

Figure 7. Comparison of current and mass responses of solutions containing complexes **1** (left panels) or **3** (right panels) as a function of time. Upper panels: gray solid lines represent applied potential; black solid lines represent current response of **1** (left) and **3** (right) recorded by the potentiostat. Dashed lines are background current. Lower panels: solid lines represent mass response in each experiment, while dashed lines are the corresponding catalyst-free backgrounds. Conditions: 0.1 M KNO_3 in air-saturated deionized water; 3 mM **1**; ca. 2.5 mM **3**. Scan rate: 50 mV/s.

still had some background variability.[30] (See the Supporting Information for electrode current and mass backgrounds.)

The EQCN results on a solution of catalyst precursor **1** during cyclic voltammetry are shown in Figure 6. The current and mass data are both displayed as a function of potential. As observed previously,[15] on the first anodic potential scan from 0.2 to 1.5 V vs NHE, a strong catalytic response is seen with onset near 1.1 V (see the Supporting Information for additional figures of cyclic voltammetry data with full current range). On the return cathodic sweep, there is a feature near 0.88 V, along with a background signal for the gold electrode near 0.95 V. On subsequent anodic scans, there is a new nondiffusional anodic peak near 0.88 V which grows in intensity on subsequent scans. This nondiffusional feature, similar to those observed with certain iridium oxides,[31] is characteristic of the deposited heterogeneous catalyst denoted **BL**, as after several minutes of continuous oxidation a blue layer can be seen forming at the electrode.

As previously reported,[15] **BL** is an amorphous iridium oxide containing a small admixture of carbon. It is remarkably active for water oxidation and is robustly adherent to the electrode surface. The catalyst forms in situ on most electrode materials (basal-plane graphite, glassy carbon, amorphous graphite, fluorine-doped tin oxide, indium-doped tin oxide, gold, and platinum). The measured overpotential is very low, on the order of 200 mV at 0.5 mA cm^{-2}. The catalyst maintains its full activity for many hours; indeed, we have seen continuous operation for periods of days without loss of activity. We have therefore focused on studying the deposition process, which has so far only been seen for the tris-aqua complex **1** and the related $[(Cp^*Ir)_2(\mu{-}OH)_3]OH$ complex.[15]

The EQCN data confirm the electrodeposition inferred from the voltammetry. On the first anodic scan, mass deposits onto the electrode surface beginning at about 1.2 V and continuing up to 1.5 V. On the return cathodic scan, mass continues to deposit until near 1.1 V, at which potential the deposition ceases and the mass on the electrode is essentially constant. This same behavior continues on subsequent passes. We monitored up to four complete cycles from 0.2 to 1.5 V and recorded a total deposition of ca. 750 ng of **BL** material onto the electrode surface. The mass increase of the electrode on subsequent scans is slightly greater than that on the first scan,

dx.doi.org/10.1021/ja2004522 |*J. Am. Chem. Soc.* 2011, 133, 10473–10481

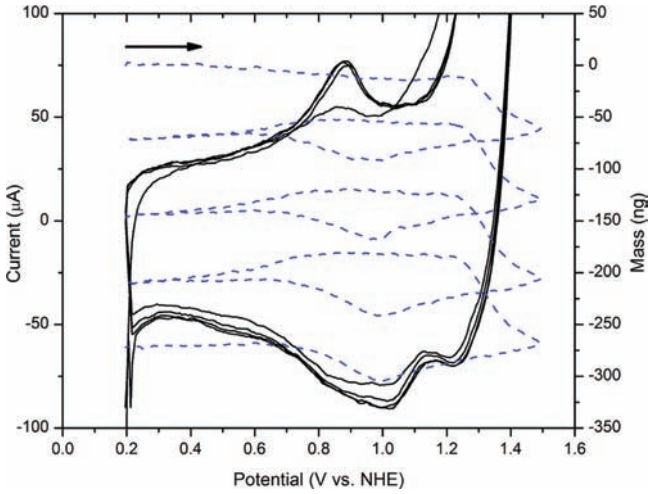

Figure 8. Response of **BL** during cyclic voltammetry as measured by EQCN. Black solid line: cyclic voltammetric response recorded by the potentiostat. Dashed blue line: mass change recorded by the nanobalance. Conditions: 0.1 M KNO_3, pH 5.5. Scan rate: 50 mV/s.

suggesting an increasing deposition rate contrary to what is seen in the case of some organic redox-active polymers, whose rate of deposition decreases as material builds up on the electrode surface.[27] Importantly, the presence of surface-bound material at these loadings is not visible to the naked eye, but easily inferred from EQCN.

The data from Figure 6 for **1** are shown again in Figure 7, left panels, for comparison with data for **3**, which are shown in the right panels. In this representation of the data for **1**, the catalytic wave clearly increases in intensity as the voltammetry progresses. This is consistent with deposition of increasing amounts of the catalyst on the surface of the electrode. The mass data show a step-function-like appearance, characteristic of the potential-dependent deposition.

Unlike **1**, **3** does not show any indications of deposition by voltammetry or EQCN. Multiple cycles between 0.2 and 1.5 V vs NHE show only the irreversible, catalytic response with an onset near 1.1 V. This process is assigned to water oxidation catalyzed by homogeneous **3**, or a soluble derivative, because the large current is not seen in the absence of catalyst (see the Supporting Information). This assignment agrees with the RRDE and Clark-electrode data (vide supra). By EQCN, the apparent mass on the electrode surface actually decreases over the course of the experiment. This is likely due to reorganization of the gold surface, as is observed in background experiments (dashed lines). Additionally, oxygen bubble formation could contribute to the apparent mass decrease (vide infra).[26]

Following the deposition experiments shown in Figures 6 and 7, we examined the deposited **BL** catalyst by EQCN in situ. Other studies have focused on the gravimetric response of iridium oxide films prepared by more traditional methods.[32,33] Our molecular precursor **1** allows us to monitor catalyst deposition in real-time and also monitor the behavior of the deposited material during catalysis. For this analysis, the electrode with deposited **BL** was rinsed and transferred to a cell with fresh electrolyte containing only 0.1 M KNO_3. The resulting behavior is shown in Figure 8.

With the response of the EQCN set to zero at the start of a cyclic voltammetry experiment (Figure 8, dashed line, upper left), on the first anodic pass, essentially no mass response is observed up to nearly 1.3 V vs NHE. This is consistent with no major catalytic activity occurring below this potential. At 1.3 V, a sizable decrease in apparent mass begins, and continues while scanning up to 1.5 V. On the return cathodic scan, the apparent mass continues to decrease until 1.0 V, at which point there is a noticeable apparent increase in mass. This mass uptake on cathodic sweep through the reversible feature near 0.85 V has been observed in EQCN studies with other iridium oxide films, and may be consistent with solvent, electrolyte, and/or proton uptake effects during reduction.[28,29] On the anodic sweeps (excluding the first), a slight mass increase is apparent on approaching the reversible feature near 0.85 V; this observation is consistent with the proton loss being accompanied by solvent water update as observed previously by EQCN for iridium oxide layers.[28,33] Otherwise, the mass response is invariant below 0.5 V, consistent with no redox processes being seen in the cyclic voltammogram. The apparent mass decrease from one cycle to the next (change in mass at 0.2 V) is due entirely to the mass changes generated above 1.2 V. This observed net mass decrease is very likely caused by bubble formation at the surface of the electrode during catalytic water oxidation, which is visible upon inspection of the electrode following the four-cycle run. Because bubble formation decreases hydrostatic pressure from the solvent on the electrode, bubble formation registers as an apparent mass decrease. Additionally, the reversible peak near 0.85 V does not vary in intensity, suggesting that little electroactive **BL** material is lost from the electrode surface during catalysis under these conditions. This apparent mass decrease does not occur when the precursor **1** is present in solution (Figure 6), because on the first few scans deposition and not water oxidation is likely the dominant process.

Previously, we have used the peak current of the reversible feature near 0.85 V to estimate the surface coverage of electroactive **BL**.[15] This method could give information only about the iridium that undergoes this redox process and consequently was inherently limited. With the mass data in hand, we can now compare estimates of electroactive iridium with the deposited mass on the electrode surface. We consider two possible limiting situations: (1) the tris-aqua cation is deposited without any significant change in mass or (2) pure iridium(IV) dioxide is deposited. Using the molecular masses to convert from nanograms to moles, and related calculations to convert the peak currents to moles (we assume a two-electron, three-proton process, as before), minimum estimates of electroactive iridium as a percentage of mass deposited can be obtained.[31] The resulting fit between the data sets (data set used comes from a four-cycle voltammetry for deposition of **BL**) is shown in the Supporting Information. In the case of the assumption that the unmodified precursor **1** is deposited, we find that the percent of iridium centers that are electroactive is 9.9%. In the case of deposition of pure iridium(IV) dioxide, we find that only 5.5% of the deposited iridium is electroactive. These numbers are consistent with previous preparations of iridium oxide electrodes, and contrast with Murray's extensively electroactive small nanoparticles of iridium dioxide.[6] However, electroactive films of iridium oxide (like our **BL**) are known to be hydrated, and studies on even bare gold electrodes forming oxides have shown that trapped water and surface oxide restructuring can give mass increases which are substantially larger than the stoichiometries of oxide formation. Consequently, these numbers represent a lower estimate of the electroactive iridium content.

DISCUSSION

The observed difference in mass response obtained for **1** and **3** obtained by EQCN effectively rules out the electrodeposition of **3** at the gold electrode on the time scale of these experiments, and strongly differentiates the behavior of **1** and **3** when driven by an electrode potential. Both complexes are molecular precursors for water-oxidation catalysis, but clearly do not function in the same manner under the conditions. Oxidation of **1** initiates formation of a heterogeneous material **BL**, which electrodeposits irreversibly and functions as a robust solid-state catalyst.[15] Based on the EQCN data and analysis (Figures 7 and 8), it is also apparent that **BL** deposits at a relatively uniform rate, which, when taken in concert with the cyclic voltammetry data, suggests that successively deposited layers contain similar electroactive iridium content, at least at the short times investigated here. We plan to exploit this understanding of the deposition rate to investigate the nature of **BL** by spectroscopy in a future report.

Conversely, **3** catalyzes water oxidation without evidence of deposition, giving dioxygen as observed by RRDE and Clark-electrode studies. **1** and **3** are oxidized at a similar potential, but their behavior could scarcely be more different. In the case of **BL**, the appearance of the reversible, nondiffusional process at 0.85 V helps to distinguish the heterogeneous material being formed. However, prefeatures before onset of catalysis may not be easy to observe in all cases. For example, our own work and that of others has shown the prefeatures in iridium oxide films to be sensitive to experimental conditions and configurations.[31]

Water-oxidation catalysis is often studied with primary chemical oxidants that provide a strong driving force for the reaction. In the case of manganese complexes such as our own $[(H_2O)(terpy)Mn(\mu\text{-}O)_2Mn(terpy)(OH_2)]^{3+}$ complex, the chemical oxidant most often used is oxone (potassium peroxymonosulfate), a two-electron oxo-donor oxidant with a potential of ca. 1.85 V vs NHE.[34] In the case of noble metal catalysts such as those of ruthenium and iridium, the one-electron oxidant cerium(IV) can often be used.[35] Cerium(IV) in the form of cerium(IV) ammonium nitrate (CAN) is only kinetically stable under very acidic (ca. pH 1) conditions and has a standard redox potential of approximately 1.7 V. CAN has a rich history of oxidative organic transformations,[36] and could contribute to oxidative decomposition of organometallic catalysts. Ligand degradation leading to iridium oxide colloids or nanoparticles likely occurs to some extent with many organometallic iridium precursors in the presence of excess ceric ion, which makes careful measurements at short times particularly important in such studies.

As we reported previously, complex **1** evolves oxygen when injected into a solution containing cerium(IV) at pH 0.89.[14] However, the kinetics of the resulting oxygen evolution are not first order in catalyst and suggest oligomerization of the precursor. This is consistent with the observation of electrode deposition at potentials greater than 1.1 V at pH 2.9.[15] Clearly, complex **1** undergoes rapid conversion to an iridium oxide material when oxidized at an electrode. This material is then active for catalytic water oxidation.[37] This feature of **1** could easily be missed in the absence of electrochemical data, and so future cerium(IV) studies could usefully be complemented with aqueous electrochemical investigations.

While EQCN can accurately monitor apparent mass changes at the electrode surface, it cannot provide data regarding the formation of soluble or suspended products, including iridium oxide nanoparticles which may form from molecular precursors. Previous studies by Murray and co-workers on small iridium oxide nanoparticles have shown that hydroxide-capped particles at high pH do not deposit on electrodes held at up to 1.2 V vs NHE, but that higher voltages (up to 1.5 V) do induce electrodeposition (by reducing the local pH near the electrode surface).[6,38] Similarly, Yagi et al. showed that larger citrate-capped iridium oxide nanoparticles spontaneously deposit onto ITO electrodes, even without application of an oxidizing potential.[39] Under the conditions of the EQCN experiment with **3** (unbuffered water, voltages up to 1.5 V), iridium oxide nanoparticles formed at the electrode would deposit and be detected as an increase in mass. The lack of such a change in the mass of the electrode does not rigorously exclude nanoparticle formation, but it does provide strong evidence against it. Importantly, the use of the EQCN in studies on oxidation catalysts provides information that has been previously unavailable. Because catalytic water oxidation has important applications in artificial photosynthesis and solar-energy storage, EQCN may help guide the development of suitable electrocatalysts.

CONCLUSIONS

Compounds **1**, **2**, and **3** have been identified as molecular water-oxidation catalyst precursors. However, the behavior of compound **1** at the surface of an electrode differs greatly from that of **3**. **3** evolves oxygen when oxidized by an electrode in aqueous solution and does not form electrodeposited material. **1** displays a prominent catalytic wave in voltammetry and is shown by EQCN to be a precursor for a heterogeneous catalyst. EQCN studies thus distinguish the homogeneous or heterogeneous nature of oxygen-evolving electrocatalysts. This is key to interpreting the true nature of the catalysts in each case, because iridium oxides are among the most effective water-oxidation catalysts known.

EXPERIMENTAL SECTION

General. All solvents were of commercial grade and dried over activated alumina using a Grubbs-type solvent purification system prior to use.[40] ^{1}H and ^{19}F NMR spectra were collected on a 400 MHz Bruker spectrometer and referenced to the residual protio-solvent signal or the deuterium lock signal in the case of ^{19}F. ^{13}C NMR spectra were collected on a 500 MHz Varian spectrometer and referenced to the solvent ^{13}C signal. δ in reported in units of ppm and J in Hz. UV−vis spectra were collected using a Varian Cary 50 Bio UV−vis spectrometer with samples in a 1.0 cm quartz cuvette at an iridium concentration of 0.20 mM at pH 7. The dissociation constant for **2** was calculated using Specfit/32.[41] Elemental analyses were performed by Atlantic Microlab, Inc. 2-(2′-Pyridyl)-2-propanol[42] and $[(\eta^5\text{-}C_5Me_5)Ir(H_2O)_3]SO_4$ (**1**)[16] were obtained according to published procedures. Crystal samples of **1** used for X-ray crystallography were obtained by slow evaporation of a concentrated aqueous solution in an unstoppered vial.

(η^5-C_5Me_5)Ir(2-(2′-Pyridyl)-2-propanolate)Cl (2). $[Cp^*IrCl_2]_2$ (0.4106 g, 0.5154 mmol), sodium bicarbonate (0.345 g, 4.11 mmol), and 2-(2′-pyridyl)-2-propanol (0.1420 g, 1.036 mmol) were combined in a 100 mL Schlenk flask with an attached reflux condenser, and 50 mL of degassed acetone was added. A rubber septum cap was fitted to the top of the reflux condenser and connected via a needle to an oil bubbler. The reaction was then heated to reflux with a slow flow of nitrogen gas through the reaction headspace for 2 h, during which time the reaction lightened in color to pale orange. The reaction then was cooled to room temperature, treated with a small quantity of anhydrous magnesium sulfate to remove excess water, and then filtered through Celite under air. The resulting solution was reduced on a rotary evaporator to a total volume of

approximately 3 mL, then capped and stored in the freezer overnight to give orange crystals that were separated from the remaining supernatant by means of a pipet and then dried in vacuo. Yield 0.416 g (81%). ^{1}H NMR (400 MHz, MeOD) δ 8.69 (dt, J = 5.2, 1.3 Hz, 1H), 7.88 (td, J = 7.9, 1.5 Hz, 1H), 7.46−7.31 (m, 2H), 1.67 (s, 15H), 1.46 (s, 6H). ^{13}C NMR (126 MHz, CD_3OD) δ 177.34, 150.97, 139.53, 125.54, 122.95, 85.97, 84.74, 33.67, 9.01. Calcd for $Ir_1C_{18}H_{25}N_1Cl_1 \cdot 0.67\ H_2O$: C, 42.30; H, 5.19; N, 2.74; O, 5.22. Found: C, 42.24; H, 5.22; N, 2.68; O, 5.25. Crystal samples used for X-ray crystallography were obtained by an alternate preparation[43] from a concentrated methylene chloride solution layered with pentane.

(η^5-C_5Me_5)Ir(2-(2′-Pyridyl)-2-propanolate)trifluoroacetate (3). (η^5-C_5Me_5)Ir(2-(2′-Pyridyl)-2-propanolate)Cl (**2**) (0.3321 g, 0.6654 mmol) and silver trifluoroacetate (0.1529 g, 0.6922 mmol) were placed in an aluminum-foil wrapped round-bottom flask under nitrogen atmosphere and 24 mL of degassed, deionized water was added via a cannula. The reaction was stirred under N_2 with continued exclusion of light for 1.5 h and then filtered through Celite quickly in air. The Celite was rinsed with an additional 5 mL of deionized water, and then the combined aqueous solutions were washed with three 80 mL portions of diethyl ether using a separatory funnel to remove excess silver trifluoroacetate. The water was then removed with a rotary evaporator to give a pure yellow-orange solid. The color of the resulting solid depends strongly on the degree of hydration. Yield 0.331 g (86% on an anhydrous basis). ^{1}H NMR (400 MHz, DMSO) δ 8.77 (d, J = 5.7 Hz, 1H), 8.10 (td, J = 7.8, 1.4 Hz, 1H), 7.59 (d, J = 8.0 Hz, 1H), 7.53 (ddd, J = 7.2, 5.8, 1.3 Hz, 1H), 1.69 (s, 15H), 1.34 (s, 6H). ^{13}C NMR (126 MHz, DMSO) δ 176.04, 157.79 (q, J = 30.4 Hz), 151.29, 140.45, 125.68, 122.54, 117.5 (q, weak, J = 300 Hz) 92.38, 85.04, 32.16, 8.42. ^{19}F NMR (376 MHz, DMSO) δ −73.3. Crystal samples used for X-ray crystallography were obtained by evaporation of a concentrated aqueous solution.

Cyclic Voltammetry. The measurements were made on a Princeton Applied Research Versastat 4-400 or model 273 potentiostat/galvanostat using a standard three-electrode configuration. A basal-plane graphite electrode (surface area: 0.09 cm^2) was used as the working electrode to minimize background oxidation current. The preparation and treatment of the basal-plane graphite electrode has been described previously.[14] A platinum wire was used as the counter electrode, and a Ag/AgCl electrode (Bioanalytical Systems, Inc.) was used as the reference (Ag/AgCl vs NHE: +197 mV). Experiments were carried out in unbuffered solutions containing 0.1 M KNO_3 (Strem Chemicals) as the supporting electrolyte. The solution pH was adjusted with dilute potassium hydroxide or nitric acid in some experiments, as noted.

Rotating Ring-Disk Electrode Electrochemistry. RRDE studies were carried out in a single-chamber cell configuration with a Pine AFCBP1 Bipotentiostat and a Pine MSR variable-speed rotator. The reference was either a Ag/AgCl electrode (Bioanalytical Systems, Inc.) or a platinum wire referenced first to Ag/AgCl, and the counter electrode was a platinum wire. The disk (surface area: 0.07 cm^2) material was basal-plane graphite (with stabilizing resin around the graphite; from Pine), and ring electrode material was platinum. The disk and ring were assembled in a Pine E6-series ChangeDisk RRDE. The theoretical maximum collection efficiency with our electrode geometry is 23.3%. Ring electrode current data was smoothed (adjacent averaging) to minimize noise.

Clark-Electrode Oxygen Detection. Real-time measurements of oxygen evolution coupled to electrochemical oxidation were made with a YSI Clark-type oxygen electrode. Prior to beginning each set of experiments, the oxygen-permeable membrane covering the commercial YSI electrode was replaced to ensure a high-quality response and complete electrical isolation of the Clark electrode from the bulk solution. The electrodes were inserted into a tight-fitting water-jacketed glass vessel with the appropriate connections for the oxygen-detecting, gold working (surface area: 0.017 cm^2) and Ag/AgCl reference electrodes, and a second chamber for the platinum counter electrode. The system was kept at a constant temperature of 25 °C. In a typical experiment, a freshly prepared electrolyte solution in Milli-Q water (7.5 mL, pH 7, 0.1 M KNO_3) was allowed to equilibrate over minutes before electrolysis was initiated. The gold electrode was polarized to 1.7 V vs NHE for approximately 10 min in the electrolyte to collect the background current and oxygen production, after which time the electrode was switched off, the catalyst injected, and the potential switched back on for ca. 10 min. This potential was necessary for the oxygen detection experiment, since we desired increased signal-to-noise and a clear temporal response from the Clark electrode. This approach allows resolution of any lag phase behavior, which we have anticipated would indicate formation of secondary materials. Basal-plane graphite electrodes are unsuitable for this experiment, as they undergo extensive oxidative damage over the timecourse required.

Electrochemical Quartz Crystal Nanobalance. Simultaneous cyclic voltammetry and piezoelectric gravimetry measurements were collected with an Elchema EQCN-600 nanobalance and an Elchema PS-605B potentiostat. Both instruments were computer-controlled with the Elchema Voltscan program (version V.4.1). A conventional three-electrode cell configuration was used; the counter electrode was a platinum foil, and an Ag/AgCl electrode (Bioanalytical Systems, Inc.) served as the reference. The working electrode was a 14 mm diameter quartz crystal (AT cut, plano−plano, 10 MHz) coated with a gold/chromium conducting surface (approximate electroactive surface area: 0.256 cm^2). The quartz crystal disk was mounted in an EQCM-5710 quartz crystal holder (Institute of Physical Chemistry, Polish Academy of Sciences, Warsaw, Poland). The frequency response of the quartz crystal was additionally monitored before and during experiments using a Fluke PM6680B high-resolution frequency counter. To minimize background noise, five-point adjacent averaging was used during data workup.

■ ASSOCIATED CONTENT

Supporting Information. NMR spectra for **2** and **3**. X-ray crystallographic details for **1**, **2**, and **3**. Additional electrochemistry data. This material is available free of charge via the Internet at http://pubs.acs.org.

■ AUTHOR INFORMATION

Corresponding Author

gary.brudvig@yale.edu; robert.crabtree@yale.edu; francis.dsouza@wichita.edu

■ ACKNOWLEDGMENT

This work was supported as part of the Argonne-Northwestern Solar Energy Research (ANSER) Center, an Energy Frontier Research Center funded by the U.S. Department of Energy, Office of Science, Office of Basic Energy Sciences under Award Number DE-PS02-08ER15944 (G.W.B., R.H.C., and J.D.B.). Further funding for synthetic work is gratefully acknowledged from the Division of Chemical Sciences, Geosciences, and Biosciences, Office of Basic Energy Sciences of the U.S. Department of Energy through grant DE-FG02-84ER13297 (R.H.C. and N.D.S.). Funding from the National Science Foundation (Grants 0804015 and EPS-0903806) and matching support from KTEC (F.D.) is additionally acknowledged. The authors thank Daryl Smith for fabrication of the electrochemical cells. N.D.S. thanks Professor Ann M. Valentine and Katherine M. Buettner for assistance and use of the UV−vis spectrometer. J.D.B. thanks Oana Luca and Karin Young for helpful discussions. Finally, the authors express their thanks to the referees for their helpful comments.

REFERENCES

(1) (a) Bard, A. J. *Ber. Bunsen-Ges. Phys. Chem.* **1988**, *92*, 1187–1194. (b) Calvin, M. *Acc. Chem. Res.* **1978**, *11*, 369–374. (c) Meyer, T. J. *Acc. Chem. Res.* **1989**, *22*, 163–170.

(2) (a) Concepcion, J. J.; Jurss, J. W.; Templeton, J. L.; Meyer, T. J. *J. Am. Chem. Soc.* **2008**, *130*, 16462–16463. (b) Cape, J. L.; Lymar, S. V.; Lightbody, T.; Hurst, J. K. *Inorg. Chem.* **2009**, *48*, 4400–4410. (c) Cape, J. L.; Siems, W. F.; Hurst, J. K. *Inorg. Chem.* **2009**, *48*, 8729–8735.

(3) Wasielewski, M. R. *Acc. Chem. Res.* **2009**, *42*, 1910–1921.

(4) (a) Harriman, A.; Thomas, J. M.; Millward, G. R. *New J. Chem.* **1987**, *11*, 757–62. (b) Mills, A. *Chem. Soc. Rev.* **1989**, *18*, 285–316.

(5) (a) Smith, W. *J. Power Sources* **2000**, *86*, 74–83. (b) Trasatti, S. *Electrochim. Acta* **2000**, *45*, 2377–2385. (c) Hayfield, P. C. S *Platinum Met. Rev.* **1998**, *42*, 27–33.

(6) Nakagawa, T.; Beasley, C. A.; Murray, R. W. *J. Phys. Chem. C* **2009**, *113*, 12958–12961.

(7) Gorlin, Y.; Jaramillo, T. F. *J. Am. Chem. Soc.* **2010**, *132*, 13612–13614.

(8) (a) Crabtree, R. *Acc. Chem. Res.* **1979**, *12*, 331–337. (b) Anton, D. R.; Crabtree, R. H. *Organometallics* **1983**, *2*, 855–859.

(9) (a) Crabtree, R. H.; Mihelcic, J. M.; Quirk, J. M. *J. Am. Chem. Soc.* **1979**, *101*, 7738–7740. (b) Crabtree, R. H.; Mellea, M. F.; Mihelcic, J. M.; Quirk, J. M. *J. Am. Chem. Soc.* **1982**, *104*, 107–113.

(10) Widegren, J. A.; Finke, R. G. *J. Mol. Catal. A: Chem.* **2003**, *198*, 317–341.

(11) Whitesides, G. M.; Hackett, M.; Brainard, R. L.; Lavalleye, J. P. P. M.; Sowinski, A. F.; Izumi, A. N.; Moore, S. S.; Brown, D. W.; Staudt, E. M. *Organometallics* **1985**, *4*, 1819–1830.

(12) (a) Lin, Y.; Finke, R. G. *Inorg. Chem.* **1994**, *33*, 4891–4910. (b) Widegren, J. A.; Bennett, M. A.; Finke, R. G. *J. Am. Chem. Soc.* **2003**, *125*, 10301–10310.

(13) Hull, J. F.; Balcells, D.; Blakemore, J. D.; Incarvito, C. D.; Eisenstein, O.; Brudvig, G. W.; Crabtree, R. H. *J. Am. Chem. Soc.* **2009**, *131*, 8730–8731.

(14) Blakemore, J. D.; Schley, N. D.; Balcells, D.; Hull, J. F.; Olack, G. W.; Incarvito, C. D.; Eisenstein, O.; Brudvig, G. W.; Crabtree, R. H. *J. Am. Chem. Soc.* **2010**, *132*, 16017–16029.

(15) Blakemore, J. D.; Schley, N. D.; Olack, G. W.; Incarvito, C. D.; Brudvig, G. W.; Crabtree, R. H. *Chem. Sci.* **2011**, *2*, 94–98.

(16) Ogo, S.; Makihara, N.; Watanabe, Y. *Organometallics* **1999**, *18*, 5470–5474.

(17) (a) Dadci, L.; Elias, H.; Frey, U.; Hoernig, A.; Koelle, U.; Merbach, A. E.; Paulus, H.; Schneider, J. S. *Inorg. Chem.* **1995**, *34*, 306–315. (b) Koelle, U. *Coord. Chem. Rev.* **1994**, *135−136*, 623–650.

(18) The corresponding trifluoromethanesulfonate salt was previously obtained by Watanabe and co-workers from organic solution.[16]

(19) Le Goff, A.; Artero, V.; Jousselme, B.; Tran, P. D.; Guillet, N.; Métayé, R.; Fihri, A.; Palacin, S.; Fontecave, M. *Science* **2009**, *326*, 1384–1387.

(20) Baffert, C.; Romain, S.; Richardot, A.; Leprêtre, J.-C.; Lefebvre, B.; Deronzier, A.; Collomb, M.-N. *J. Am. Chem. Soc.* **2005**, *127*, 13694–13704.

(21) Cady, C. W.; Shinopoulos, K. E.; Crabtree, R. H.; Brudvig, G. W. *Dalton Trans.* **2010**, *39*, 3985–3989.

(22) Sawyer, D. T.; Sobkowiak, A.; Roberts, J. L., Jr. *Electrochemistry for Chemists*, 2nd ed.; Wiley: New York, 1995.

(23) Bruckenstein, S.; Feldman, G. A. *J. Electroanal. Chem.* **1965**, *9*, 395–399.

(24) Park-Gehrke, L. S.; Freudenthal, J.; Kaminsky, W.; DiPasquale, A. G.; Mayer, J. M. *Dalton Trans.* **2009**, 1972–1983.

(25) Brewster, T. P.; Blakemore, J. D.; Schley, N. D.; Incarvito, C. D.; Hazari, N.; Brudvig, G. W.; Crabtree, R. H. *Organometallics* **2011**, *30*, 965–973.

(26) (a) Buttry, D. A.; Ward, M. D. *Chem. Rev.* **1992**, *92*, 1355–79. (b) Bard, A. J.; Faulkner, L. R. *Electrochemical Methods: Fundamentals and Applications*, 2nd ed.; Wiley: Hoboken, NJ, 2001.

(27) Subbaiyan, N. K.; Obraztsov, I.; Wijesinghe, C. A.; Tran, K.; Kutner, W.; D'Souza, F. *J. Phys. Chem. C* **2009**, *113*, 8982–8989.

(28) Birss, V. I.; Elzanowska, H.; Gottesfeld, S. *J. Electroanal. Chem. Interfacial Electrochem.* **1991**, *318*, 327–33.

(29) Bock, C.; Birss, V. I. *J. Electroanal. Chem.* **1999**, *475*, 20–27.

(30) Schumacher, R.; Borges, G.; Kanazawa, K. K. *Surf. Sci. Lett.* **1985**, *163*, L621–L626.

(31) (a) Burke, L. D.; Scannell, R. A. *Platinum Met. Rev.* **1984**, *28*, 56–61. (b) Burke, L. D.; Whelan, D. P. *J. Electroanal. Chem.* **1984**, *162*, 121–41.

(32) Juodkazyte, J.; Sebeka, B.; Stalnionis, G.; Juodkazis, K. *Electroanalysis* **2005**, *17*, 1734–1739.

(33) Jung, Y.; Lee, J.; Tak, Y. *Electrochem. Solid-State Lett.* **2004**, *7*, H5–H8.

(34) (a) Limburg, J.; Vrettos, J. S.; Liable-Sands, L. M.; Rheingold, A. L.; Crabtree, R. H.; Brudvig, G. W. *Science* **1999**, *283*, 1524–1527. (b) Kurz, P.; Berggren, G.; Anderlund, M. F.; Styring, S. *Dalton Trans.* **2007**, 4258–4261. (c) Limburg, J.; Vrettos, J. S.; Chen, H.; de Paula, J. C.; Crabtree, R. H.; Brudvig, G. W. *J. Am. Chem. Soc.* **2000**, *123*, 423–430.

(35) (a) Concepcion, J. J.; Jurss, J. W.; Brennaman, M. K.; Hoertz, P. G.; Patrocinio, A. O. v. T.; Murakami Iha, N. Y.; Templeton, J. L.; Meyer, T. J. *Acc. Chem. Res.* **2009**, *42*, 1954–1965. (b) Romain, S.; Vigara, L.; Llobet, A. *Acc. Chem. Res.* **2009**, *42*, 1944–1953.

(36) Nair, V.; Deepthi, A. *Chem. Rev.* **2007**, *107*, 1862–1891.

(37) The catalytic properties of **1** before oligomerization or deposition to form **BL** are currently under investigation.

(38) Nakagawa, T.; Bjorge, N. S.; Murray, R. W. *J. Am. Chem. Soc.* **2009**, *131*, 15578–15579.

(39) Yagi, M.; Tomita, E.; Sakita, S.; Kuwabara, T.; Nagai, K. *J. Phys. Chem. B* **2005**, *109*, 21489–21491.

(40) Pangborn, A. B.; Giardello, M. A.; Grubbs, R. H.; Rosen, R. K.; Timmers, F. J. *Organometallics* **1996**, *15*, 1518–1520.

(41) (a) Gampp, H.; Maeder, M.; Meyer, C. J.; Zuberbuhler, A. D. *Talanta* **1985**, *32*, 95–101. (b) Gampp, H.; Maeder, M.; Meyer, C. J.; Zuberbuhler, A. D. *Talanta* **1985**, *32*, 257–264. (c) Gampp, H.; Maeder, M.; Meyer, C. J.; Zuberbuhler, A. D. *Talanta* **1985**, *32*, 1133–1139. (d) Gampp, H.; Maeder, M.; Meyer, C. J.; Zuberbuhler, A. D. *Talanta* **1986**, *33*, 943–951.

(42) Wong, Y.-L.; Yang, Q.; Zhou, Z.-Y.; Lee, H. K.; Mak, T. C. W.; Ng, D. K. P. *New J. Chem.* **2001**, *25*, 353–357.

(43) In the alternate preparation, $[Cp^*IrCl_2]_2$ (0.101 g, 0.127 mmol), sodium acetate (0.092 g, 1.1 mmol), and 2-(2′-pyridyl)-2-propanol (0.36 g, 0.26 mmol) were stirred for 3 h at room temperature under nitrogen in 10 mL of acetone, then filtered through celite, reduced, and crystallized. The tendency of the product acetic acid to co-crystallize with the iridium complex led to the replacement of sodium acetate with sodium bicarbonate in subsequent preparations.